Solid-State Additive Manufacturing of Shape-Memory Ceramic Reinforced Composites

Donald J. Erb[1], Nikhil Gotawala[1], Hang Z. Yu[1*]

[1] Department of Materials Science and Engineering, Virginia Tech, Blacksburg, VA 24061, USA.

[*] Corresponding Author: hangyu@vt.edu

Abstract

We report a solid-state additive manufacturing route for producing shape-memory ceramic ($Zr_{0.88}Ce_{0.12}O_2$) reinforced metal matrix composites. Using additive friction stir deposition, we implement two feedstock engineering strategies: (i) pre-mixing of powders using a Cu matrix and (ii) hole-pattern drilling using an Al-Mg-Si matrix, where the specific matrix materials are chosen for their distinct shear flow behaviors. The process yields fully dense composites with uniform particle dispersion (20 vol%) and dynamically recrystallized metal matrices. Severe thermomechanical conditions also reduce the ceramic particle size, resulting in unique composite microstructures unattainable by alternative processing routes. The as-printed composites withstand high compressive loads without cracking and retain functionality enabled by thermally and mechanically triggered martensitic transformations. Notably, for the first time, stress-induced martensitic transformation (tetragonal to monoclinic) is observed in bulk-scale composites—but it is only present in the Cu matrix composite, not the Al-Mg-Si counterpart. Micromechanics modeling attributes this contrast to differences in the load transfer and strain hardening capabilities. Complementary to global transformation characterization, Raman mapping reveals that transformation typically initiates at the particle-matrix interface. Together, these results establish a potential pathway for scalable manufacturing of multi-functional metal–shape memory ceramic composites with tunable microstructures and transformation responses.

Keywords: Shape memory ceramics; additive friction stir deposition; metal matrix composites; stress-induced martensitic transformation; interface chemical reaction; Raman spectroscopy mapping

1. Introduction

With a wide range of tunable operating temperatures [1, 2], ZrO_2-based shape memory ceramics exhibit shape memory and superelastic functionality through reversible tetragonal–monoclinic transformations under thermal, mechanical, or electrical stimuli [3, 4]. In micro-pillar or particle form, they demonstrate high energy dissipation densities (on the order of 100 MJ/m^3) and excellent functional fatigue resistance [2,5]. However, scaling to the bulk form remains difficult due to their large transformation strain and intrinsic brittleness [6]. Approaches to mitigate this issue include using single crystals to eliminate intergranular mismatch stresses [1, 7] or tailoring composition and lattice parameters to create more compatible interfaces with reduced hysteresis [8–11]. Beyond monolithic forms, mesostructure engineering offers alternative solutions by minimizing mechanical constraint against martensitic transformation, such as micro-honeycombs [12–14] and granular packings [5, 15–17]. Among various mesostructure forms, metal matrix composites offer an effective balance between load-bearing capacity and functional responses. By embedding single- or oligocrystalline shape memory ceramic particles in a ductile matrix, the resulting composites are expected to exhibit structural performance and stimulus-driven transformations concurrently [18–21].

Figs. 1A and 1B illustrate three possible transformation paths for these composites. Type I involves thermally induced transformation: ceramic particles begin in the austenite (tetragonal) phase and transform to martensite (monoclinic) upon cooling, which is reversible by heating [18,19]. Such behavior is promising for adaptive thermal management systems and components that respond to temperature changes. In Type II, ceramic particles in a metastable austenite phase transform to martensite during mechanical loading and retain martensite after unloading, with reversibility upon heating [19]. This mode is attractive for one-time energy absorption applications, where subsequent thermal reset is possible. Type III begins with stable austenite, transforming to martensite during loading and partially reverting to austenite upon unloading. This mode enables partial strain recovery and energy dissipation under cyclic loading. While Types II and III resemble the shape memory and superelastic effects of individual particles, plastic deformation of the metal matrix limits such effects at the composite level. These composites, therefore, are better suited for sensing, damping, structural health monitoring, and energy dissipation, while maintaining strong structural performance for multi-functional applications [21]. Compared to conventional, non-transforming metal matrix composites, they additionally provide tunable, reversible martensitic transformations that open new pathways for adaptive and stimulus-responsive structural applications.

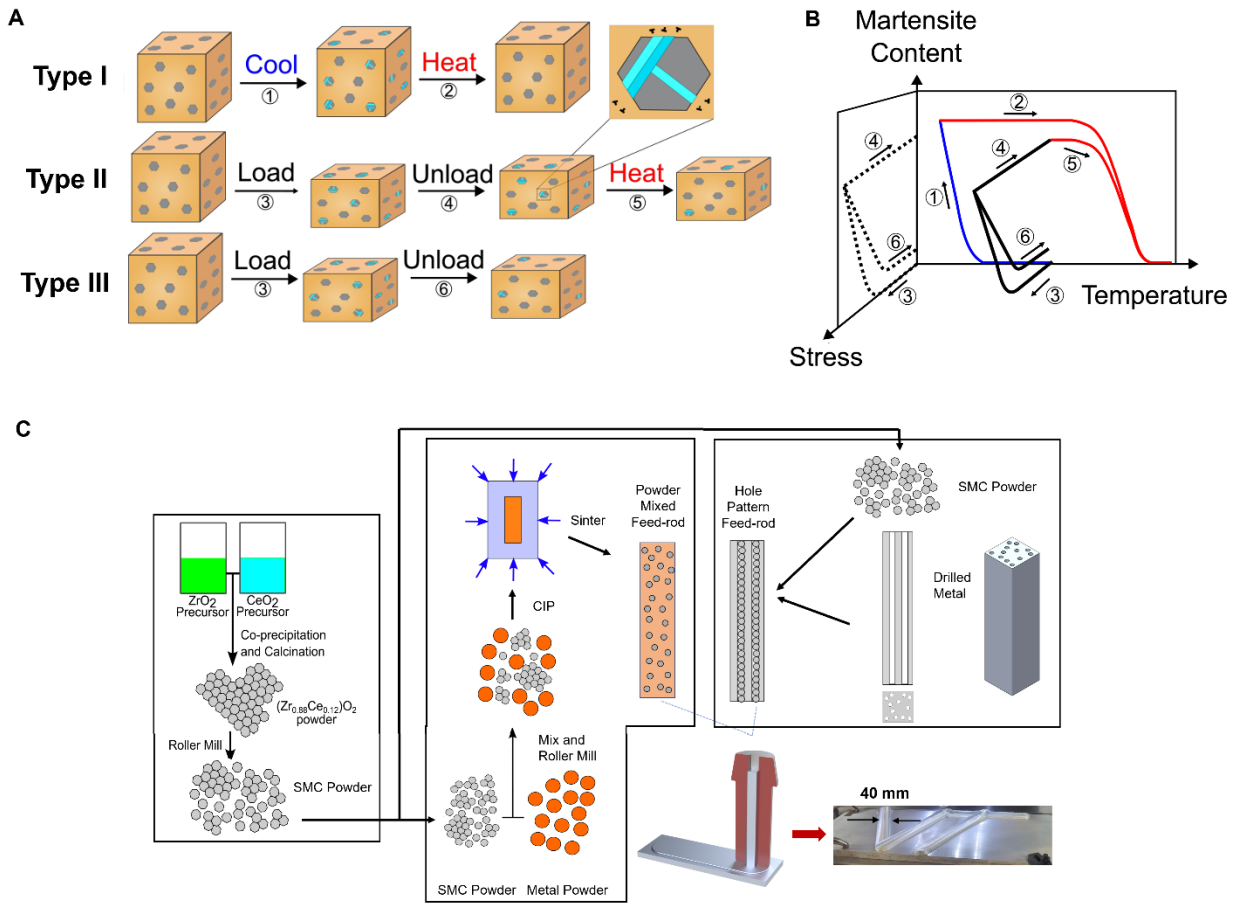

Fig. 1. Transformation paths of the composites and processing routes for feedstock engineering. (A) The idealized stress-induced and cooling-induced behavior of metal matrix-shape memory ceramic composites. (B) The corresponding transformation pathways through stress and temperature. (C) Procedures for printing composites using AFSD, involving pre-mixing and hole pattern-drilling methods for feed-rod preparation.

The major challenge of using metal matrix-shape memory ceramic composites lies in manufacturing. It is non-trivial to simultaneously achieve uniform ceramic dispersion, strong interfacial bonding, and full density on the bulk level. Consequently, despite earlier conceptual proposals of their transformation behavior, experimental validation has only recently emerged. Via powder processing, Zheng *et al.* successfully achieved >99% dense Al-ceria-zirconia composites with 16.2 vol% ceramic [19], and pioneeringly demonstrated stress-induced martensitic transformation in micro-pillars (with particle alignment) fabricated from these composites. This exciting observation confirms functional responses of the mesostructured composite form and motivates broader exploration with critical questions to be answered. Fundamentally, why was stress-induced martensitic transformation *not observed in bulk-scale composites* [18, 19]? While the use of submicron particles could elevate the critical transformation stress [22], the characteristics of the Al matrix may also inhibit load transfer and suppress transformation in individual ceramic particles. Gaining mechanistic insights requires scalable manufacturing

strategies to conveniently produce high-quality composites that endure large applied strains and accommodate a range of matrix materials beyond Al.

Here, we present a solid-state additive manufacturing approach for metal–shape memory ceramic composites using additive friction stir deposition (AFSD) [23, 24]. Compared to alternative processing routes for metal matrix composites, AFSD is a shear-driven process that leverages intense mechanical stirring and matrix flow to produce fully dense composites with good dispersion and interface quality. Demonstrated in conventional metal matrix composites [25, 26], these capabilities make AFSD an ideal platform for shape memory ceramic–metal systems, because uniform particle distribution and robust interfaces are vital for reliable, repeatable martensitic transformations. Using feedstock engineered by pre-mixing or hole-pattern drilling (Fig. 1C), we demonstrate centimeter-scale composites containing 20 vol% shape memory ceramics in either Cu or Al-Mg-Si matrices. Dynamic recrystallization of the matrix material, size reduction of ceramic particles, as well as interface chemical reaction and phase transformation are found to occur during deposition, resulting in unique composite microstructures. Remarkably, for the first time, stress-induced martensitic transformation is observed in bulk-scale composites; it is found in the Cu matrix composite but remains absent in the Al-Mg-Si counterpart. This contrast is attributed to load transfer differences governed by the strain hardening capability and flow stress level of the matrix.

2. Materials and Methods

2.1 Feedstock Engineering and Composite Manufacturing

$(Zr_{0.88}Ce_{0.12})O_2$, in a metastable austenite phase at room temperature, was selected as the shape memory ceramic to enable *ex situ* phase characterization after cooling- or stress-induced martensitic transformation. $(Zr_{0.88}Ce_{0.12})O_2$ powder was synthesized using co-precipitation and calcination as detailed elsewhere [15]. After calcination, the $(Zr_{0.88}Ce_{0.12})O_2$ powder was roller milled with zirconia media to obtain single crystals or oligocrystals. Two feedstock engineering methods were employed: powder pre-mixing and hole-pattern drilling. These were demonstrated using Cu and Al-Mg-Si (AA6061) matrices, respectively, selected for their contrasting rotational flow behaviors in AFSD. Cu was known to exhibit minimal rotation, necessitating pre-mixing in the feed-rod; Al-Mg-Si underwent significant rotational flow to enable *in situ* mixing, making it suitable for the hole-pattern drilling method [27].

For pre-mixing, $(Zr_{0.88}Ce_{0.12})O_2$ and Cu powders (-325 mesh, Fisher Scientific) were mixed and roller milled for 24 hours, followed by cold isostatic pressing and sintering at 880 °C for 3 hours in ultra-high-purity argon to form the feed-rod. For hole-pattern drilling, an Al-Mg-Si (AA6061) feed-rod was drilled at designed locations and packed with $(Zr_{0.88}Ce_{0.12})O_2$ powder. Before AFSD, the shape memory ceramics in feed-rods contained ~15-20 vol% martensite. Both feed-rods (12.7 mm × 12.7 mm in cross-section) were then inserted into the print head of an AFSD system. With a print head rotation rate of 450–600 RPM and in-plane velocity of 3 mm/s, wall structures of Cu and Al-Mg-Si composites—each approximately 10 mm tall, 40 mm wide, and 100 mm long—were

built on Cu and AA6061 plates, respectively (see Supplemental Fig. S1 for print morphology and Fig. S2 for temperature recordings during AFSD). Multiple samples were cut from the printed walls for characterization. For cooling-induced martensitic transformation, samples were submerged in liquid nitrogen (–196 °C) for 30 minutes after bubbling ceased. For stress-induced transformation, cylindrical samples were quasi-statically compressed up to 1000 MPa engineering stress (Instron 4468).

2.2 Phase and Microstructure Characterization

The microstructures of Cu and Al-Mg-Si composites were characterized by scanning electron microscopy (SEM), electron backscatter diffraction (EBSD), and transmission electron microscopy (TEM), using Helios 5 UC and Titan microscopes. The ceramic particle size distributions were obtained from dynamic light scattering and high contrast SEM imaging. The relative densities of composites were calculated using the Archimedes method with water as the medium. Global phase characterization was conducted using X-ray diffraction (XRD, Bruker D8 Advance) with Cu Kα radiation; the martensite volume fraction, V_M, within $(Zr_{0.88}Ce_{0.12})O_2$ was calculated based on intensities of the tetragonal (101) and monoclinic (111) and $(11\bar{1})$ peaks using [10, 28]:

$$X_M = \frac{I_{M(11\bar{1})} + I_{M(111)}}{I_{M(11\bar{1})} + I_{M(111)} + I_{T(101)}} \quad (1)$$

$$V_M = \frac{1.311\, X_M}{1 + 0.311\, X_M} \quad (2)$$

Local phase transformation was characterized using Raman spectroscopy mapping (Horiba XploRA PLUS confocal microscope, 532 nm wavelength) with a 2 μm step size. Raman spectra corresponding to the metal matrices were removed using principal component analysis and Gaussian mixture model clustering [29]; the martensite fraction in the remaining $(Zr_{0.88}Ce_{0.12})O_2$ spectra was quantified using multivariate curve resolution-alternating least squares (MCR-ALS) [30].

3. Microstructural Characteristics Resulting from AFSD

3.1 Cu Matrix Composite by Pre-mixing

Density measurements and SEM characterization confirm that both the as-printed Cu and Al-Mg-Si matrix composites are fully dense. Fig. 2 presents the microstructure of the Cu-$(Zr_{0.88}Ce_{0.12})O_2$ composite (hereafter Cu-SMC, where SMC denotes shape memory ceramic). After calcination, the ceramic exhibits a grain size of approximately 2-5 μm. Following ball milling, most ceramic particles are reduced to a few microns, which is comparable to the grain size. This indicates that they are single crystal or oligocrystalline [5, 15]. However, some larger particles, tens of microns in size, remain and are composed of multiple grains, thus classified as polycrystalline. Fig. 2A shows representative examples of both particle types within the as-printed Cu-SMC composite.

Inverse pole figure (IPF) maps in Figs. 2B and 2C compare the Cu matrix between the pre-mixed feedstock and the as-printed composite. The feed-rod exhibits a grain size of 3.0 ± 1.9 μm and a high density of annealing twins, as expected for sintered Cu. The presence of ceramic particles introduces geometrically necessary dislocations (GNDs) in the Cu matrix during cooling due to their thermal coefficient mismatch [31]. This is observed by the higher kernel average misorientation (KAM) values near particles, which are non-indexed regions in Figs. 2B-C. The printed composite shows a uniform microstructure with significantly refined grains, reduced to 1.1 ± 0.5 μm. This is because in printing metal matrix composites via AFSD, the metal matrix undergoes rapid, intense plastic deformation at elevated temperatures. The peak temperature is typically above 60% of its melting point, resulting in viscoplastic flow and dynamic recrystallization [25, 32]. The Cu grain size distribution before and after AFSD is compared in Fig. 2D.

However, the peak temperature during printing remains relatively low for the ceramic phase—below 30% of zirconia's melting point in this work. As a result, the ceramics behave in a brittle manner and fracture under large shear during deposition. This extensive brittle fracture leads to significant ceramic particle size reduction during printing, as shown in Figs. 2E and 2F, consistent with prior reports [32, 33]. This fragmentation is beneficial, as single-crystal ceramic particles are preferred over polycrystalline ones due to the absence of grain boundaries, enabling reversible martensitic transformation without fracture [1, 2, 12].

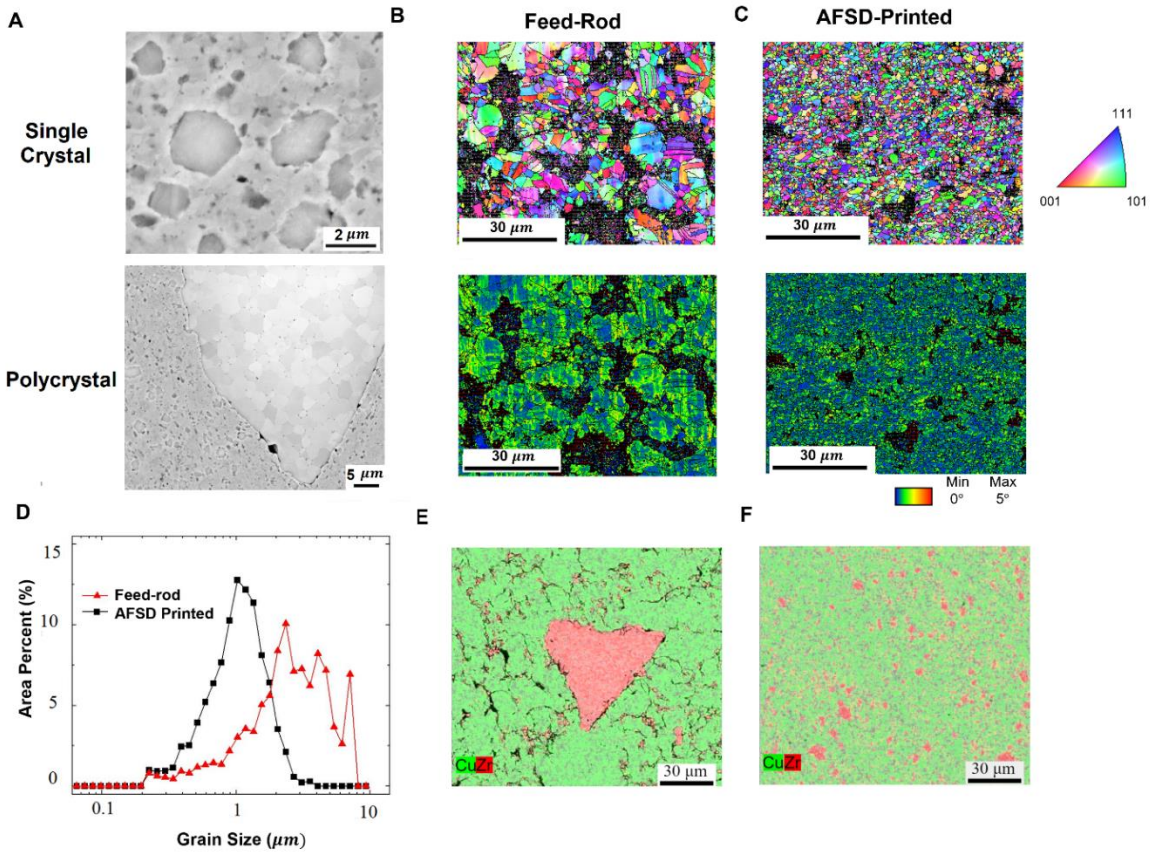

Fig. 2. Microstructure of the Cu-SMC composite. (A) SEM micrographs showing single crystal and polycrystalline ceramic particles after deposition. IPF and KAM maps are compared between the (B) feed-rod and (C) printed composite. (D) Cu grain size distribution before and after deposition. EDS (energy dispersive spectroscopy) mappings of Cu and Zr are compared (E) before and (F) after deposition, highlighting particle size reduction and dispersion.

3.2 Al-Mg-Si Matrix Composite by Hole-Pattern Drilling

Fig. 3 shows the microstructure of the Al-Mg-Si-SMC composite, which is fabricated by drilling hole patterns in the feed-rod. While hole-drilling is common in AFSD [24, 26, 32], the relationship between hole locations and final particle distribution has been elusive. Figs. 3A-C compare three feed-rod patterns and their resulting particle distributions along the height of deposition. Key to such designs is the material flow behavior (upper in Fig. 3D): the outer feed-rod material deposits in upper/outer regions, while the center material accumulates at the bottom, as known from AFSD modeling and experiments [34, 35]. Building on this understanding, Fig. 3C presents an optimized pattern with uniform radial distribution. The resulting improvement in particle dispersion is evident (lower in Fig. 3D), where the height-wise particle distribution is compared among the three designs. All subsequent results of the Al-Mg-Si-SMC composite uses this optimized configuration.

Like in the Cu-SMC composite, the Al-Mg-Si matrix undergoes substantial grain refinement during AFSD, as evidenced by IPF and KAM maps (Figs. 3E-F). The average grain size drops from $128.7 \pm 53.8\ \mu m$ (feed-rod) to $15.1 \pm 5.9\ \mu m$ (deposit), with the grain size distributions compared in Fig. 3G. Regions near ceramic particles (non-indexed areas in Fig. 3F) exhibit further grain refinement due to grain boundary pinning, while containing high densities of GNDs [32]. The ceramic particles also undergo size reduction due to shear-induced fracture during deposition (Figs. 3H-I), showing good dispersion in the printed Al-Mg-Si composite.

Overall, both AFSD feedstock engineering methods enable the fabrication of fully dense materials even from partially dense feed-rods. Meanwhile, they refine the grain and particle sizes and ensure uniform distribution due to extreme thermomechanical processing. It should be emphasized that Al-Mg-Si is selected for the hole-pattern drilling method because its favorable flow during AFSD yields a uniform particle distribution across the deposition cross-section. In contrast, Cu exhibits asymmetric flow and is better suited for pre-mixing. To examine this aspect in more detail, hole drilling is also attempted for Cu using the same pattern, but particle accumulation on the advancing side produces uneven cross-sections (Supplemental Fig. S3). Such heterogeneity generates local stress concentrations and hinders consistent martensitic transformation, thereby reducing the reproducibility of shape-memory and superelastic responses in bulk composites.

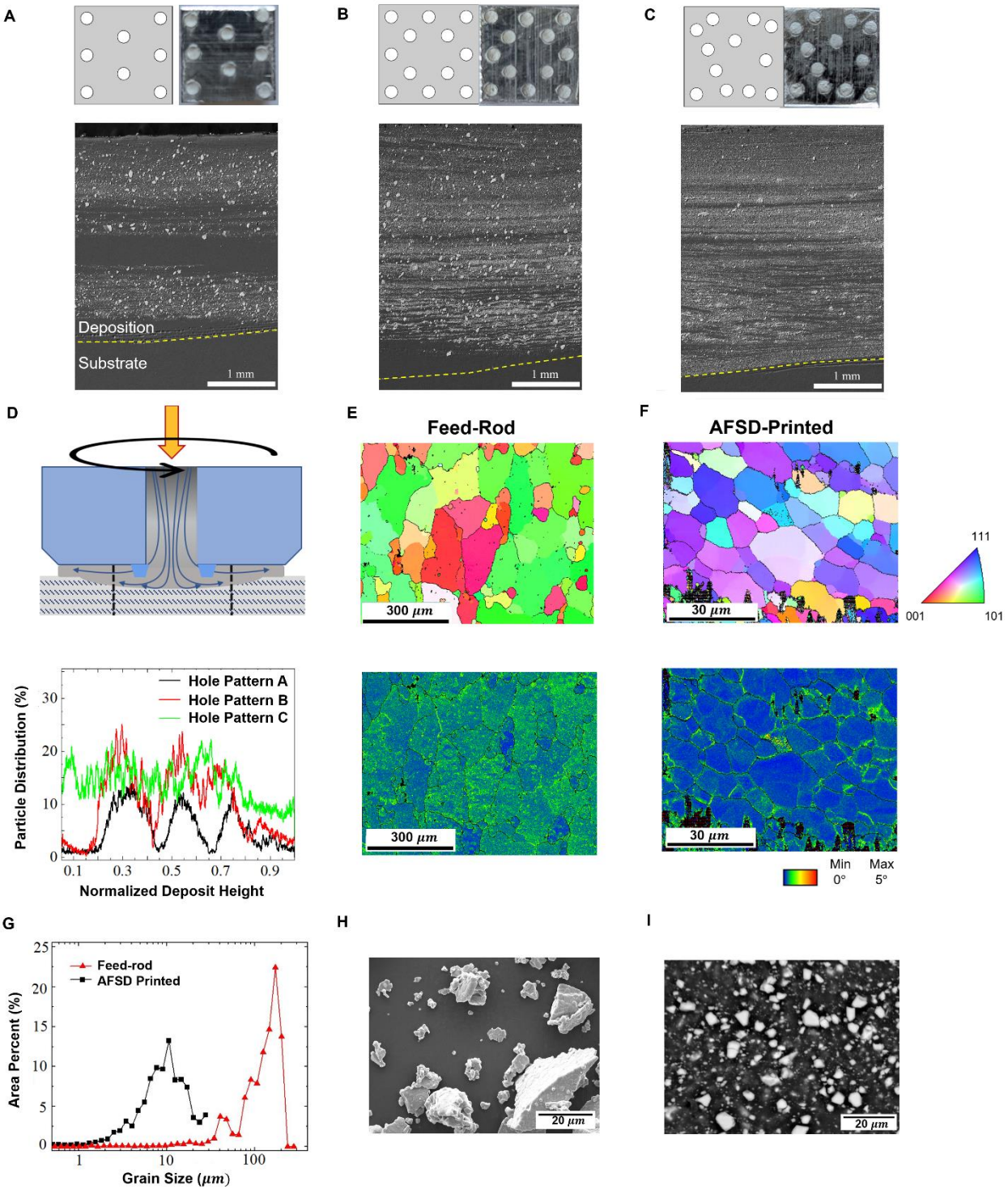

Fig. 3. Microstructure of the Al-Mg-Si-SMC composite. (A-C) Three hole patterns used in this study and the resulting particle distribution after AFSD. (D) Upper: illustration of material flow in AFSD; Lower: measured particle distribution along the height for different hole patterns. IPF and KAM maps are compared between the (E) feed-rod and (F) printed composite. (G) Al grain size distribution before and after deposition. SEM micrographs are compared between (H) the powder used for packing the feed-rod and (I) the dispersed ceramic particles in the printed composite.

3.3 Interface Chemical Reaction

Given the critical role of interfacial bonding in maximizing the load bearing capacity and implementing functional responses, we employ TEM to examine the interface structure between the ceramic particle and metal matrix. For the Cu-SMC system (Figs. 4A and 4B), the interface between the ceramic particle and Cu is sharp, with negligible interdiffusion as seen from chemical element mapping. For the Al-Mg-Si-SMC system (Figs. 4C and 4D), in contrast, a thin MgO layer is observed on the ceramic particle surface. Such MgO layers are not present in the feedstock, so they must be formed during AFSD, which has a thermomechanical processing nature. Formation of thin MgO layers on ceramic particles has also been observed in other works when ZrO_2 particles (or other oxides like TiO_2 and Al_2O_3) are incorporated into Al alloys containing Mg as a major alloying element [21, 26, 36-38]. High-resolution TEM images (Figs. 4E and 4F) confirm that no new phase forms between the Cu matrix and the ceramic, whereas a thin (<10 nm) amorphous interlayer develops at the interface in the Al-Mg-Si-SMC composite. This layer is chemically bonded to both the matrix and ceramic, providing strong interfacial cohesion. The ceramic near the interface remains crystalline after AFSD, with the tetragonal phase confirmed by FFT analysis (Fig. 4G).

The formation of a stable MgO shell in Al-Mg-Si-SMC and the lack of a similar copper oxide shell in Cu-SMC can be understood by comparing the formation energies of various oxides based on the Ellingham diagram [39]. In the Cu-SMC system (Fig. 4H), the formation of a Cu_2O interface would be energetically unfavorable compared to ZrO_2 across the entire peak temperature range (shaded region) encountered during AFSD of Cu composites. Therefore, no interface chemical reaction occurs. In the Al-Mg-Si-SMC system, Mg (0.8-1.2 wt%) and Si (0.4-0.8 wt%) are the primary alloying elements in the matrix. As shown in Fig. 4I, MgO is the most energetically stable oxide, while SiO_2 remains energetically unfavorable relative to ZrO_2 across the entire peak temperature range. During AFSD, therefore, Mg solute atoms in the Al matrix diffuse toward the metal–ceramic interface and react with ZrO_2 particles to form a thin MgO interfacial layer. The formation of other stable oxide layers, e.g., the aluminum oxide observed by Zheng *et al.*, can also be rationalized accordingly [19].

In addition to the MgO interfacial layer, Fig. 4D shows a precipitate particle formed through diffusional phase transformation. Enriched in Cu and Si but lacking Mg, this precipitate is likely to be the Q phase commonly observed in Al-Mg-Si alloys. Its formation, rather than the more typical β or β' phases, can be attributed to local compositional changes caused by Mg depletion, as Mg atoms are primarily consumed in the interfacial reaction. Interestingly, the MgO layer forms directly on the ceramic particle surface while the precipitate forms on the MgO layer, indicating that the interfacial chemical reaction precedes precipitation, as discussed below.

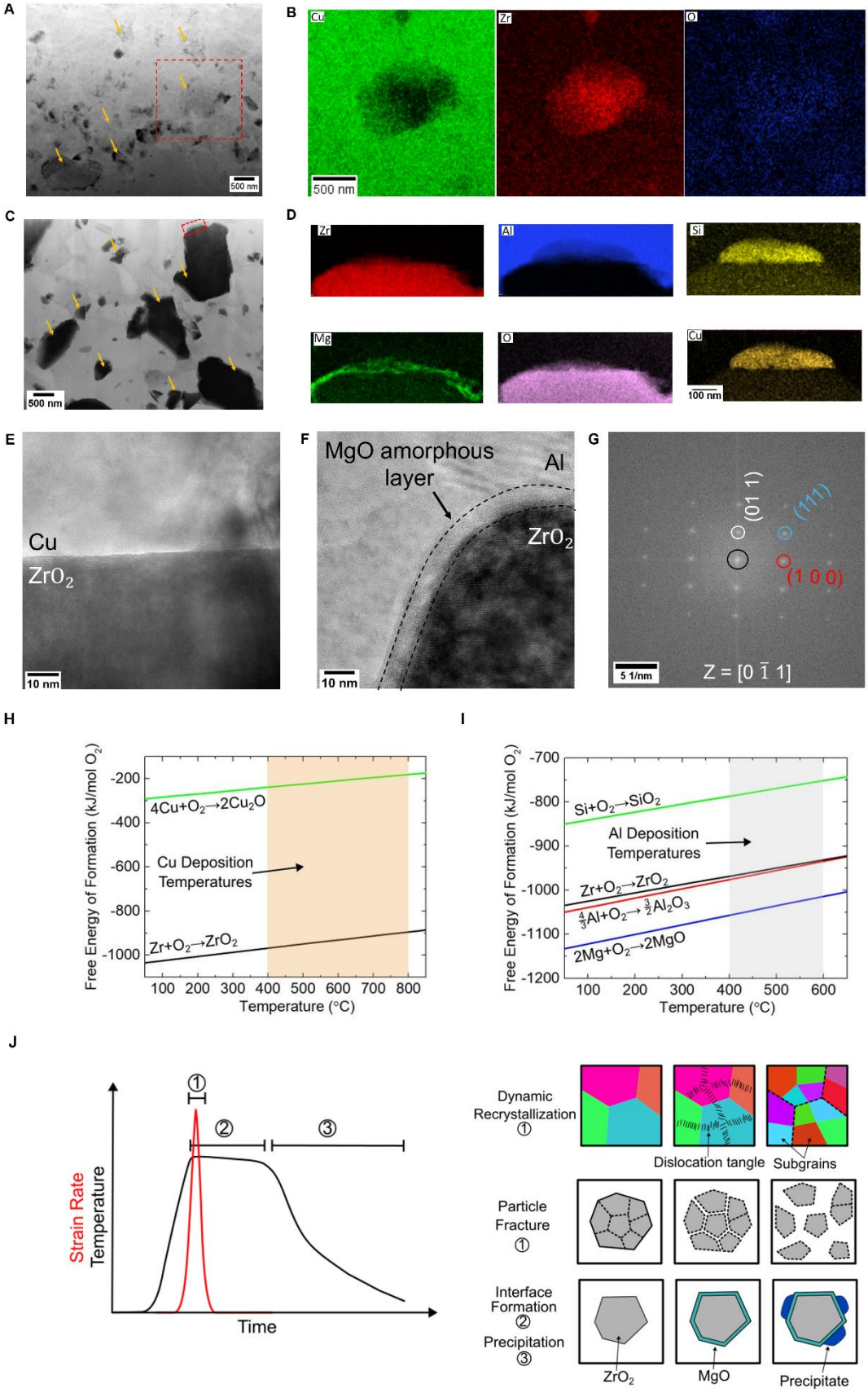
A
500 nm
B
Cu
Zr
O
500 nm
C
500 nm
D
Zr
Al
Si
Mg
O
Cu
100 nm
E
Cu
ZrO2
10 nm
F
MgO amorphous layer
Al
ZrO2
10 nm
G
(0 1 1)
(111)
(1 0 0)
5 1/nm
Z = [0 1̄ 1]
H
Free Energy of Formation (kJ/mol O2)
4Cu+O2→2Cu2O
Cu Deposition Temperatures
Zr+O2→ZrO2
Temperature (°C)
I
Free Energy of Formation (kJ/mol O2)
Si+O2→SiO2
Al Deposition Temperatures
Zr+O2→ZrO2
4/3Al+O2→2/3Al2O3
2Mg+O2→2MgO
Temperature (°C)
J
Strain Rate
Temperature
Time
Dynamic Recrystallization ①
Dislocation tangle
Subgrains
Particle Fracture ①
Interface Formation ②
Precipitation ③
ZrO2
MgO
Precipitate

Fig. 4. Interface chemical reaction. Bright-field TEM images are shown for (A) the Cu-SMC and (C) Al-Mg-Si-SMC composites, with arrows highlighting the ceramic particles. Corresponding high-magnification EDS maps are shown for (B) Cu-SMC and (D) Al-Mg-Si-SMC, probing potential new phase formation at the interfaces. High-resolution TEM images of the interfacial regions are presented for (E) Cu-SMC and (F) Al-Mg-Si-SMC composites, with the FFT analysis of the SMC particle near the interface shown in (G). Ellingham diagrams are compared for the (H) Cu-ZrO_2 and (I) Al-Mg-Si-ZrO_2 systems, with typical temperatures during AFSD shaded. (J) Diagram is drawn for the thermomechanical processing history of individual material voxels during AFSD, with the resulting microstructure evolution phenomena illustrated.

3.4 Dynamic Microstructure Evolution Phenomena during AFSD

Based on the observations in this work, Fig. 4J summarizes the overall microstructural evolution of these composites. During AFSD, the metal undergoes a complex 3D flow path, experiencing a short period of rapid, severe plastic deformation at elevated temperatures ('1' in the processing history plot) [34]. The large strain combined with high temperature results in dynamic recrystallization typically involving grain subdivision, followed by subgrain rotation to form fine grains [23, 27]. Meanwhile, the ceramic particles are sheared at a low homologous temperature, leading to fracture and particle size reduction. After that, the material remains under the print head for an extended period at high temperature with minimal deformation ('2'), allowing chemical reactions to occur between the metal matrix and ceramic particles, such as MgO shell formation. Once deposition is complete, the material—no longer beneath the print head—enters the wake of the traveling print head and begins a prolonged cooling period ('3'). As the temperature drops below a critical threshold, precipitates can nucleate, with the ceramic particle surface, now covered by a MgO shell, serving as heterogeneous nucleation sites.

4. Functional Responses

4.1 Thermally Induced Martensitic Transformation: Cyclic Behavior and Local Transformation Characteristics

With their microstructural features unraveled, we next examine the functional responses of the printed composites, focusing on Type I and Type II transformation paths. For Type I, thermal cycling is performed between 450 °C and -196 °C for up to 11 cycles. As shown in Fig. 5A, upon reaching the maximum temperature, the ceramic particles in both Cu and Al-Mg-Si composites fully transform into the austenite (tetragonal) phase. However, upon cooling to the minimum temperature, the $(Zr_{0.88}Ce_{0.12})O_2$ particles in the Cu matrix form 18.6 vol% martensite (monoclinic), compared to only 7.2 vol% in the Al-Mg-Si matrix. Thermally induced martensitic transformation is governed by differences in chemical and strain energy [10]. Since the ceramic composition is identical in both composites, the disparity in transformation volume likely arises from strain energy variations due to the matrix constraint, which depend on thermal expansion mismatch and interfacial strength [40]. The thermal expansion coefficients of Cu (17×10^{-6} K^{-1}) and Al (23×10^{-6} K^{-1}) are relatively similar, so thermal mismatch and the resulting residual stress effect cannot explain the observation. Instead, the reduced transformation in the Al-Mg-Si composite can be

attributed to the formation of MgO interfacial layer, which binds the ceramic particles and increases the shear strain energy required for transformation.

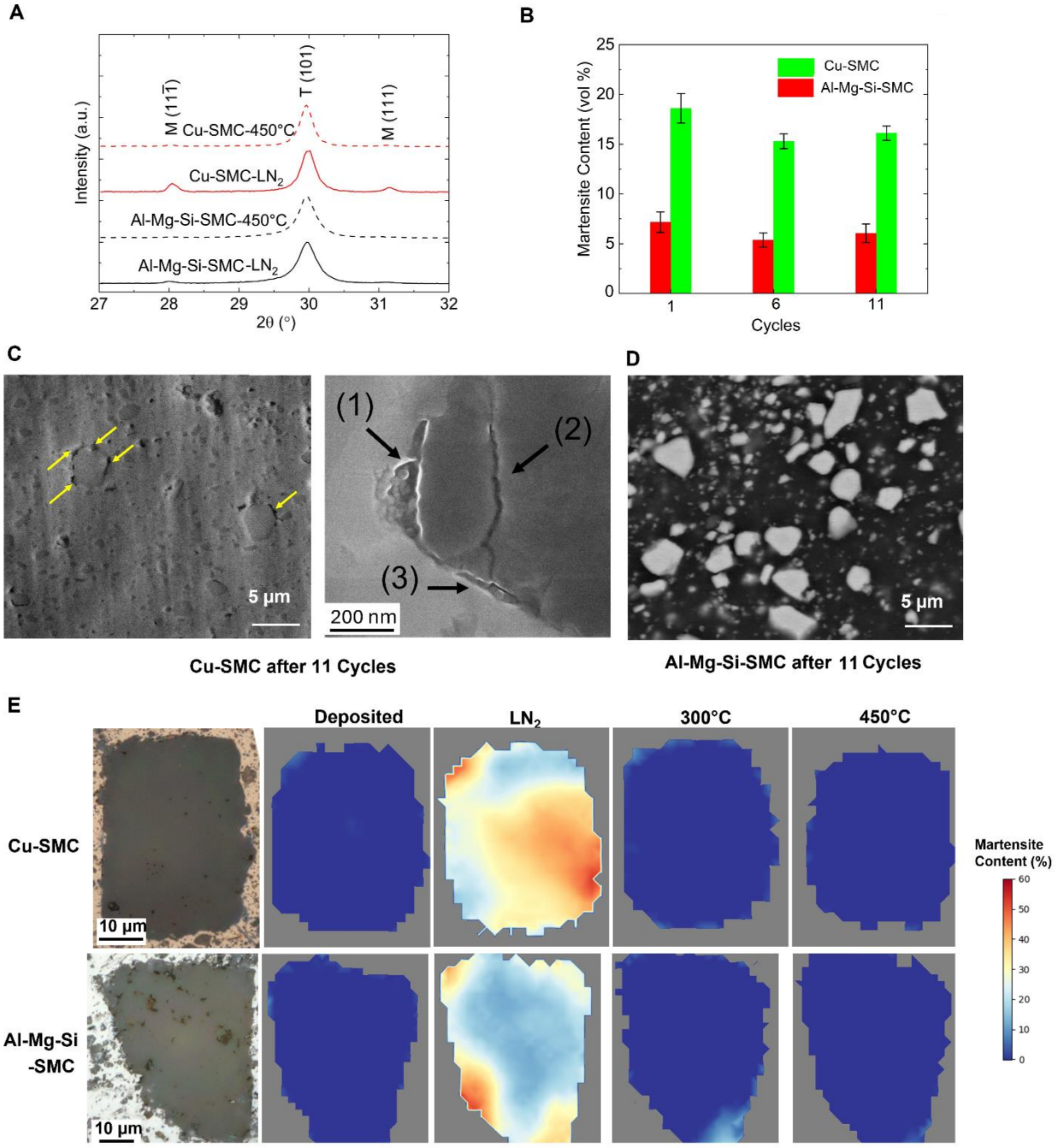

Fig. 5. Thermally induced forward and reverse martensitic transformation in composites. (A) Martensite content after the first 450 °C/ -196 °C thermal cycle. (B) Martensite content of the bulk composites after various cycles. Microstructures after 11 thermal cycles are shown for (C) Cu-SMC (left: low magnification; right: high magnification image highlighting damage sites and types) and (D) Al-Mg-Si-SMC composites. (E) Raman spectroscopy maps illustrate the local transformation behavior during a single thermal cycle.

Throughout 11 thermal cycles, both Cu and Al-Mg-Si composites exhibit minimal changes in martensite content (Fig. 5B) and no observable structural damage, demonstrating robust functional stability without degradation. This low functional fatigue behavior is attributed to the use of single- or oligocrystalline ceramic particles, which lack extensive grain boundaries or triple junctions, and the relatively small transformation volume in each cycle. This contrasts with bulk-scale monolithic shape memory ceramics, which typically fracture after only a few cycles due to large transformation strains [9]. Post-cycling microstructural analysis further supports this stability. In the Cu-SMC composite, minor interfacial defects are occasionally observed (left image in Fig. 5C), likely caused by thermal expansion mismatch or the volumetric change during martensitic transformation. High-resolution examination reveals distinct damage types: (1) interface debonding, (2) internal fracture of the SMC particle, and (3) internal cracks parallel to the interface, which can cause partial separation of the SMC particle from the interfacial region even when the interface remains intact. These damage types, indicated by arrows and labels in the right image of Fig. 5C, facilitate local stress relief. In contrast, the Al-Mg-Si-SMC composite (Fig. 5D) maintains well-bonded interfaces, owing to the lower transformation extent in thermal cycling and the MgO layer formation that enhances interfacial strength.

To gain spatially resolved insight into the transformation behavior, Raman spectroscopy mapping is performed during thermal cycling [12]. Examples are shown in Fig. 5E, where the ceramic particles begin predominantly in the tetragonal (austenite) phase. Upon cooling to –196 °C, partial transformation to the monoclinic (martensite) phase occurs, with a substantially higher degree observed in the Cu-SMC composite. This is consistent with the global transformation findings. In both composites, martensite is maximal at the particle–matrix interface and decreases radially inward, suggesting martensite nucleation at the interface. This may result from local stress concentrations that enhance the driving force or from interfacial defects and partial debonding that reduce energy barriers via local stress relaxation. Upon heating to 300 °C, most martensite reverts to austenite, except for small regions near the interface, indicating that the austenite start temperature is below 300 °C. By 450 °C, the transformation is nearly complete, in agreement with global phase evolution observed by XRD. EBSD analysis of tetragonal SMC grains before and after cryogenic transformation shows no significant texture evolution (Supplemental Fig. S4). This indicates that multiple habit plane variants are activated without a strong orientation preference. The transformation reversibility is likely controlled by interfacial constraints rather than by crystallographic texture effects.

4.2 Stress Induced Martensitic Transformation in Bulk-Scale Cu-$(Zr_{0.88}Ce_{0.12})O_2$ Composite

In this section, Type II transformation path is examined for the printed composites. Based on XRD, Figs 6A-6C compare the global martensite content in $(Zr_{0.88}Ce_{0.12})O_2$ particles as a function of applied engineering stress. In the Cu-SMC composite, the martensite volume remains largely unchanged up to 500 MPa but increases significantly at 750 MPa and 1000 MPa, indicating the onset and progression of stress-induced martensitic transformation. The increasing transformation volume with applied stress aligns with the predicted continuous transformation mode [41] and

represents the first and only observation of stress-induced transformation in bulk-scale metal–$(Zr_{0.88}Ce_{0.12})O_2$ composites. Upon annealing to 600 °C, the martensite reverts to the initial content, completing the reversible Type II transformation path. In contrast, no transformation is observed in the Al-Mg-Si-SMC composite throughout compression, consistent with the prior report for $(Zr_{0.88}Ce_{0.12})O_2$ constrained in pure Al [19]. Note after peak stress loading, both composites remain intact without surface cracking, suggesting good manufacturing quality using the proposed methods (Supplemental Fig. S5).

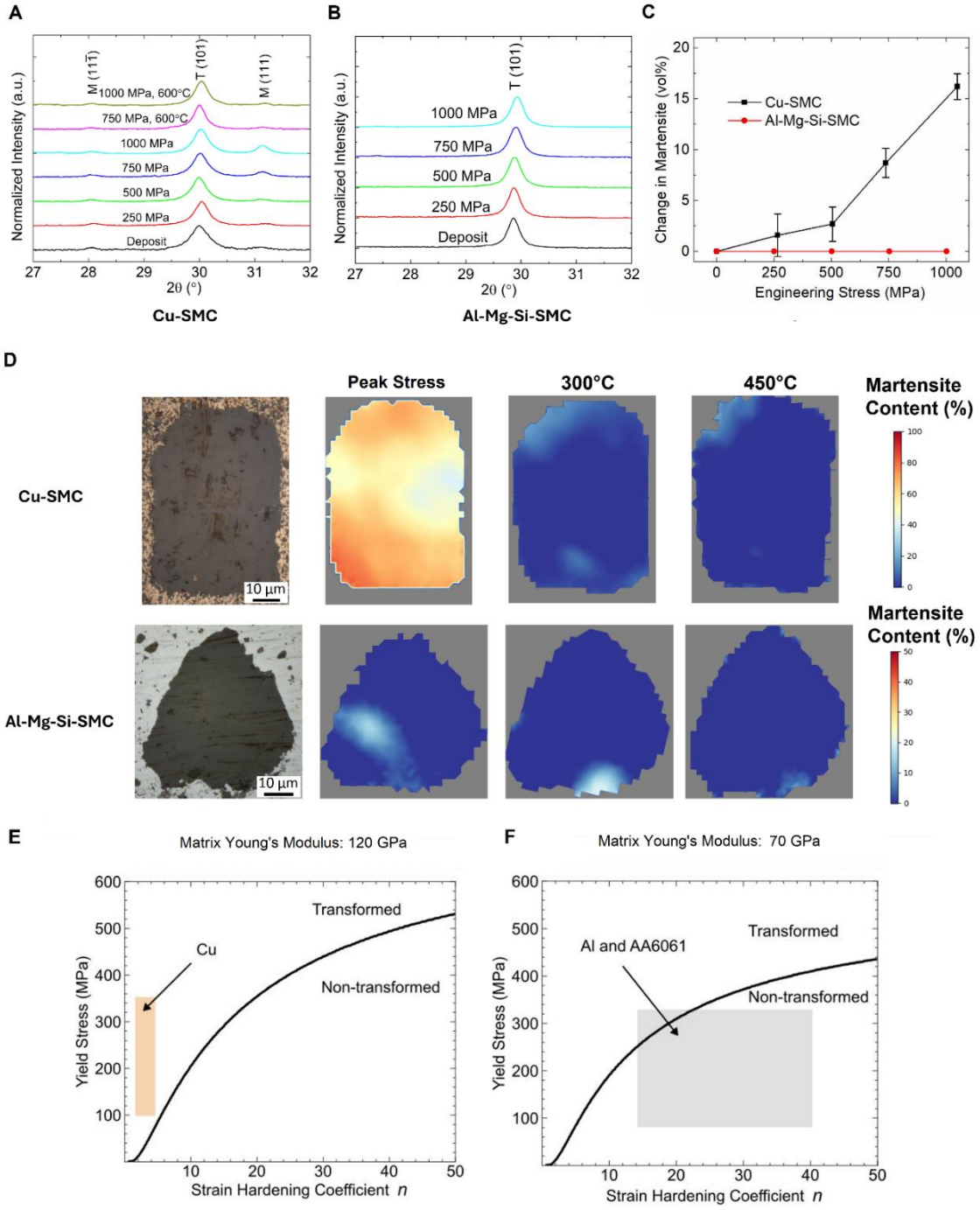

Fig. 6. Stress induced martensitic transformation in composites. XRD results are compared between (A) Cu-SMC and (B) Al-Mg-Si-SMC composites at various loads and after annealing. (C) Change in martensite content in the ceramic particles as a function of the applied loads. (D) Raman mappings showing local transformation events after loading and subsequent heating. Based on micromechanics modeling, transformation maps for 20 vol% of ceramic particles are calculated for (E) Cu matrix and (F) Al-Mg-Si matrix, covering engineering stress levels up to 1000 MPa. Shaded regions represent literature values for the yield stress and the strain hardening coefficient of these two materials. Note that strong strain hardening capability corresponds to a lower value of the Ramberg–Osgood strain hardening coefficient.

Fig. 6D presents Raman spectroscopy mappings that reveal localized transformation behavior after peak stress. Consistent with XRD results, the Cu-SMC composite shows significantly more stress-induced martensitic transformation in its ceramic particles. Although the Al-Mg-Si-SMC composite exhibits negligible global transformation, localized martensite formation still occurs in some larger particles, as evidenced here. Such minor transformations occur only in isolated regions and are not widespread. This indicates that the overall transformed volume fraction is very low—likely below the XRD detection limit. Upon heating to 300 °C, both composites undergo near-complete reversion to austenite, but further heating to 450 °C still leaves residual martensite near the particle–matrix interface. This behavior mirrors the thermally induced case in Fig. 5E, where the highest martensite fraction forms near the interface, and these regions could be the last to revert upon heating. The persistence of interfacial martensite suggests that mechanical constraints imposed by the matrix play a critical role in transformation of these ceramic particles. Here, owing to the spatial resolution constraint, the Raman characterization examples shown in Figs. 5 and 6 focus on large polycrystalline particles, where autocatalytic effects may occur. This contrasts with oligocrystalline particles, which tend to transform more coherently. Nevertheless, the initiation of transformation at the particle–matrix interface is expected to remain a common feature.

4.3 Role of Load Transfer

Given the similarities in ceramic chemistry and particle volume fraction, the stark difference in stress-induced martensitic transformation is primarily governed by differences in load transfer between Cu and Al-Mg-Si composites, which is inherently linked to the matrix properties. The high transformation stress of individual ceramic particles requires the metal matrix to plastically deform during mechanical loading, so effective load transfer depends on whether the matrix can sustain high stress without yielding excessively, i.e., possessing high yield stress or strong strain hardening capability.

This notion can be quantitatively evaluated using micromechanics modeling, which analyzes elastic and plastic deformation via the Ramberg–Osgood relationship:

$$\varepsilon = \frac{\sigma}{E} + 0.002 \left(\frac{\sigma}{\sigma_y}\right)^n, \tag{3}$$

where E is the elastic modulus, σ_y is the 0.2% offset yield stress, and n is the Ramberg-Osgood strain hardening coefficient [42-44]. Starting from an unstressed state, if the applied stress is incrementally increased by $\Delta\sigma_a$, the current tangent moduli of the matrix E_m and particle E_p can be calculated separately based on their curves of Eq. 3. Following Corbin and Wilkinson [42] in modeling isotropic particulate composites, the current tangent modulus of composite E_c can be determined with given particle (V_p) and matrix (V_m) volume fractions:

$$3{E_c}^2 + \left[\left(2 - 5V_p\right)E_p + (2 - 5V_m)E_m\right]E_c - 2E_mE_p = 0 \quad (4)$$

With E_m, E_p, and E_c, the stress and strain values of the matrix and particle are then updated using partitioning equations. After that, the tangent moduli of the matrix and particle for the next step are calculated. As detailed in Supplementary Materials, this procedure will be repeated at each stress increment, recalculating tangent moduli at each step and ultimately providing the particle stress evolution throughout loading.

This micromechanics model establishes a stress-induced martensitic transformation criterion by comparing the critical transformation stress and the stress transferred to ceramic particles, which is critically dependent on matrix properties (E, σ_y, and n). Assuming a critical transformation stress of 1000 MPa for $(Zr_{0.88}Ce_{0.12})O_2$ micro-particles [4, 45, 46], Figs. 6E–6F show the calculated transformation maps for Cu and Al-Mg-Si matrices with 20 vol% ceramic particles. These maps are applicable up to an engineering stress of 1000 MPa, matching the experimental loads. Aligning with qualitative analysis, transformation is seen to favor higher σ_y and lower n (stronger strain hardening). Shaded regions (based on typical values for Cu, Al, and AA6061 [43, 44, 47-50]) reveal that the Cu-SMC composite lies in the transformed zone, while most Al alloy values avoid transformation—indicating that the matrix plasticity dominates over stress transfer to particles. To further support this interpretation, aging of the Al-Mg-Si matrix followed by compression at 1000 MPa is found to produce a measurable stress-induced transformation around 4.0 vol% due to the yield strength increase (see Supplemental Fig. S6).

The present formulation applies to filler contents up to ~30 vol% (see Supplemental Fig. S7 for transformation maps at another volume fraction). Beyond that, percolation effects would require alternative modeling. For instance, prior work has used force chain mechanics to analyze transformation in micropillars with interconnected particle pathways [19]. By contrast, the bulk composites studied here contain low to moderate ceramic fractions and rely on matrix-mediated load transfer rather than force chain mechanisms. The analysis in this work can, in principle, be extended to ceramic or polymer matrices with appropriate constitutive equations in place of Eq. 3. The x-axis strain-hardening coefficient in Figs. 6E–6F represents the inverse of strain-hardening capability and serves as a tunable design parameter, enabling adjustment of matrix properties through thermal treatment or strain-rate control to achieve targeted transformation responses. The calculated particle stresses are averaged values, whereas actual stresses vary with particle size and morphology, creating local stress concentrations that may trigger transformation, as observed in the Al-Mg-Si-SMC Raman mappings. While the present micromechanics description serves as a first-order guide, it establishes a foundation for future systematic studies varying particle size,

shape, and volume fraction to develop a comprehensive predictive model linking particle geometry, local stress distribution, and transformation thresholds.

Finally, it should be noted that the composites examined here are not designed for superelasticity or cyclic energy dissipation (Type III in Fig. 1A), which would require alternative shape memory ceramic compositions such as $(Zr_{0.84}Ce_{0.16})O_2$. In contrast to shape memory ceramic micropillars or granular packings, composites are expected to exhibit pronounced functional fatigue primarily due to permanent deformation of the matrix. Nonetheless, the functional responses of both Cu-SMC and Al-Mg-Si-SMC under cyclic loading (Supplemental Fig. S8) reveal substantial plastic energy dissipation, driven by the combined contributions of matrix plasticity and, in the case of Cu-SMC, stress-induced martensitic transformation. Thermal cycling shows a broadened transformation strain over a wide temperature range. These features suggest that the present composites may be well-suited for multi-functional applications that combine structural performance with energy absorption, vibration damping, or adaptive thermal management.

5. Conclusions

This study establishes a scalable pathway for manufacturing metal matrix–shape memory ceramic ($(Zr_{0.88}Ce_{0.12})O_2$) composites using AFSD, a shear-driven additive process that yields fully dense composites with uniform particle dispersion. Two feedstock engineering routes are demonstrated using Cu and Al-Mg-Si matrices, respectively, selected for their contrasting rotational flow behaviors. The extreme thermomechanical processing condition of AFSD leads to grain refinement in the metal matrix, ceramic particle size reduction, and interface chemical reaction, resulting in a distinct composite microstructure compared to traditional powder processing. The as-printed composites sustain high compressive loading without surface cracking or large-scale defects, while retaining functional responses enabled by thermally and mechanically induced martensitic transformations. Critically, we report the first direct observation of stress-induced martensitic transformation in bulk-scale composites, specifically in the Cu-matrix system. To compare, the absence of such transformation in the Al-Mg-Si matrix composite is attributed to inadequate load transfer. From micromechanical modeling, metal matrices with high strain-hardening capacity and flow stress are essential for enabling stress-induced martensitic transformations.

These physical insights can guide future work aimed at designing both the metal matrix and shape-memory ceramic to achieve targeted, application-driven performance. For one-time energy-dissipating applications, such as impact barriers, matrices with moderate yield strength and pronounced strain hardening can be engineered so that transformation occurs in concert with significant plastic energy dissipation. For superelastic and cyclic applications, stress-induced transformation should occur with minimal permanent deformation of the matrix, favoring high-strength metals such as steels or Ti-6Al-4V. On the ceramic side, particle size and dopant chemistry can be tailored to lower the critical transformation stress and broaden the range of compatible matrices. Interface design is equally critical: interfaces must balance structural integrity with compliance to accommodate shear strains from martensitic transformation. Collectively, these

strategies could enable composites for novel multi-functional applications where mechanical performance and transformation-driven functionality are synergistically integrated.

Acknowledgement

The authors acknowledge financial support from the National Science Foundation (CMMI-1853893) and the DEVCOM Army Research Laboratory (W911NF2520067). This work was performed in part at the Nanoscale Characterization and Fabrication Laboratory, which is supported by the Virginia Tech National Center for Earth and Environmental Nanotechnology Infrastructure (NanoEarth), a member of the National Nanotechnology Coordinated Infrastructure (NNCI), supported by NSF (ECCS 1542100 and ECCS 2025151). The authors would like to thank Dr. Helge Heinrich for help with TEM imaging.

References

[1] I.R. Crystal, A. Lai, C.A. Schuh, J. Am. Ceram. Soc. 103 (2020) 4678-4690.
[2] A. Lai, Z. Du, C.L. Gan, C.A. Schuh, Science 341 (2013) 1505-1508.
[3] A. Lai, C.A. Schuh, Phys. Rev. Lett. 126 (2021) 015701.
[4] P.E. Reyes-Morel, J.-S. Cherng, I.W. Chen, J. Am. Ceram. Soc. 71 (1988) 648-657.
[5] Z. Du, X.M. Zeng, Q. Liu, C.A. Schuh, C.L. Gan, Acta Mater. 123 (2017) 255-263.
[6] I.W. Chen, P.E. Reyes-Morel, J. Am. Ceram. Soc. 69 (1986) 181-189.
[7] V.V. Osiko, M.A. Borik, E.E. Lomonova, Synthesis of Refractory Materials by Skull Melting Technique, in: G. Dhanaraj, K. Byrappa, V. Prasad, M. Dudley (Eds.), Springer Handbook of Crystal Growth, Springer Berlin Heidelberg, Berlin, Heidelberg, 2010, pp. 433-477.
[8] E.D.L. Pang, G.B. Olson, C.A. Schuh, Acta Mater. 213 (2021).
[9] E.L. Pang, C.A. McCandler, C.A. Schuh, Acta Mater. 177 (2019) 230-239.
[10] E.L. Pang, G.B. Olson, C.A. Schuh, J. Am. Ceram. Soc. 104 (2020) 1156-1168.
[11] E.L. Pang, G.B. Olson, C.A. Schuh, Nature 610 (2022) 491-495.
[12] L.K. Quinn, R. Esteves, P. Latorre-Suárez, G.R. Rossman, S. Raghavan, K.T. Faber, Acta Mater. 281 (2024) 120340.
[13] X. Zeng, N. Arai, K.T. Faber, Adv. Eng. Mater. 21 (2019) 1900398.
[14] H.A. Rauch, H.C. Cui, K.P. Knight, R.J. Griffiths, J.K. Yoder, X.Y. Zheng, H.Z. Yu, Addit. Manuf. 52 (2022).
[15] H.Z. Yu, M. Hassani-Gangaraj, Z.H. Du, C.L. Gan, C.A. Schuh, Acta Mater. 132 (2017) 455-466.
[16] J.F. Peters, M. Muthuswamy, J. Wibowo, A. Tordesillas, Phys. Rev. E 72 (2005).
[17] T.S. Majmudar, R.P. Behringer, Nature 435 (2005) 1079-1082.
[18] W. Zheng, L. Zhao, S. Jia, L. Li, Y. Liu, Y. Han, X. Chen, X. Jin, C.L. Gan, Q. Guo, Acta Mater. 276 (2024) 120118.
[19] W. Zheng, Y. Shi, L. Zhao, S. Jia, L. Li, C.L. Gan, D. Zhang, Q. Guo, Nat. Commun. 14 (2023) 7103.
[20] R.S. Lakes, T. Lee, A. Bersie, Y.C. Wang, Nature 410 (2001) 565-567.
[21] S. Jia, Z. Wangshu, L.D.W. Hao, L. Linghai, Z. Lei, G.C. Lip, Q. and Guo, Mater. Res. Lett. 13 (2025) 51-59.
[22] P.F. Becher, K.B. Alexander, A. Bleier, S.B. Waters, W.H. Warwick, J. Am. Ceram. Soc. 76 (1993) 657-663.
[23] R.S. Mishra, R.S. Haridas, P. Agrawal, Sci. Technol. Weld. Joining 27 (2022) 141-165.
[24] H.Z. Yu, Additive Friction Stir Deposition, Elsevier, 2022.

[25] R.J. Griffiths, M.E.J. Perry, J.M. Sietins, Y. Zhu, N. Hardwick, C.D. Cox, H.A. Rauch, H.Z. Yu, J. Mater. Eng. Perform. 28 (2019) 648-656.
[26] Q. Qiao, Y. Lin, D. Guo, C.T. Kwok, H.C. Qian, Z. Li, D. Zhang, L.M. Tam, J. Alloys Compd. 1026 (2025) 180501.
[27] R.J. Griffiths, D. Garcia, J. Song, V.K. Vasudevan, M.A. Steiner, W. Cai, H.Z. Yu, Materialia 15 (2021) 100967.
[28] H. Toraya, M. Yoshimura, S. Somiya, J. Am. Ceram. Soc. 67 (1984) C-119-C-121.
[29] F. Pedregosa, G. Varoquaux, A. Gramfort, V. Michel, B. Thirion, O. Grisel, M. Blondel, P. Prettenhofer, R. Weiss, V. Dubourg, J. Vanderplas, A. Passos, D. Cournapeau, M. Brucher, M. Perrot, É. Duchesnay, J. Mach. Learn. Res. 12 (2011) 2825–2830.
[30] I. Idarraga, M. Mermoux, C. Duriez, A. Crisci, J.P. Mardon, Oxid. Met. 79 (2013) 289-302.
[31] N.M. Chelliah, H. Singh, M.K. Surappa, Mater. Chem. Phys. 194 (2017) 65-76.
[32] K.V.M. Krishna, S.M. Patil, S. Sharma, S.S. Joshi, Y. Jin, M. Radhakrishnan, N.B. Dahotre, Mater. Sci. Eng. A 910 (2024) 146840.
[33] J.J. Lopez, M.B. Williams, T.W. Rushing, J.B. Jordon, P.G. Allison, G.B. Thompson, J. Mater. Res. Technol. 33 (2024) 8063-8070.
[34] N. Gotawala, H.Z. Yu, Journal of Manufacturing Processes 101 (2023) 114-127.
[35] M.E.J. Perry, H.A. Rauch, R.J. Griffiths, D. Garcia, J.M. Sietins, Y. Zhu, Y. Zhu, H.Z. Yu, Materialia 18 (2021) 101159.
[36] H. Sonomura, T. Ozaki, K. Katagiri, Y. Hasegawa, T. Tanaka, J. Ceram. Soc. Jpn. 127 (2019) 127-130.
[37] F. Khodabakhshi, A. Simchi, A.H. Kokabi, P. Švec, F. Simančík, A.P. Gerlich, Mater. Sci. Eng. A 642 (2015) 215-229.
[38] F. Khodabakhshi, A.P. Gerlich, A. Simchi, A.H. Kokabi, Mater. Sci. Eng. A 620 (2015) 471-482.
[39] M. Chase, NIST-JANAF Thermochemical Tables, 4th Edition, American Institute of Physics, 1998.
[40] R.C. Garvie, M.V. Swain, J. Mater. Sci. 20 (1985) 1193-1200.
[41] D.J. Erb, H.A. Rauch, K.P. Knight, H.Z. Yu, Shape Mem. Superelast. (2023).
[42] S.F. Corbin, D.S. Wilkinson, Acta Metall. Mater. 42 (1994) 1311-1318.
[43] R.C. Rice, J.L. Jackson, J. Bakuckas, S. Thompson, Metallic Materials Properties Development and Standardization, Battelle Memorial Laboratories, Columbus, 2003.
[44] S. Wiese, F. Kraemer, J.A. Ahmar, The onset of plastic flow in copper materials used for rigid and flexible PCB, 2017 18th International Conference on Thermal, Mechanical and Multi-Physics Simulation and Experiments in Microelectronics and Microsystems (EuroSimE), 2017, pp. 1-5.
[45] P.E. Reyes-Morel, I.-W. Chen, J. Am. Ceram. Soc. 71 (1988) 343-353.
[46] Z. Du, X.M. Zeng, Q. Liu, A. Lai, S. Amini, A. Miserez, C.A. Schuh, C.L. Gan, Scripta Mater. 101 (2015) 40-43.
[47] L. Li, X.J. Zhu, L. Zhang, F.Z. Tian, Journal of Physics: Conference Series 2045 (2021) 012013.
[48] M. Kouzeli, D.C. Dunand, Acta Mater. 51 (2003) 6105-6121.
[49] Y.W. Yan, L. Geng, A.B. Li, Mater. Sci. Eng. A 448 (2007) 315-325.
[50] W.F. Hickey, K. Ravi-Chandar, Transition from Flat to Slant Fracture in Ductile Materials, in: G. Hütter, L. Zybell (Eds.), Recent Trends in Fracture and Damage Mechanics, Springer International Publishing, Cham, 2016, pp. 215-235.